

The Y-Band at 1.035 μm : Photometric Calibration and the Dwarf Stellar / Sub-stellar Color Sequence

Lynne A. Hillenbrand, Jonathan B. Foster

California Institute of Technology

lah@astro.caltech.edu

S.E. Persson

Observatories of the Carnegie Institution of Washington

K. Matthews

California Institute of Technology

ABSTRACT

We define and characterize a photometric bandpass (called “Y”) that is centered at 1.035 μm , in between the traditionally classified “optical” and “infrared” spectral regimes. We present Y magnitudes and Y-H and Y-K colors for a sample consisting mostly of photometric and spectral standards, spanning the spectral type range sdO to T5V. Deep molecular absorption features in the near-infrared spectra of extremely cool objects are such that the Y-H and Y-K colors grow rapidly with advancing spectral type especially from late M through mid L, substantially more rapidly than J-H or H-K which span a smaller total dynamic range. Consistent with other near-infrared colors, however, Y-H and Y-K colors turn blueward in the L6-L8 temperature range with later T-type objects having colors similar to those of warmer M and L stars. Use of the Y-band filter is nonetheless promising for easy identification of low-mass stars and brown dwarfs, especially at young ages. The slope of the interstellar reddening vector within this filter is $A_Y = 0.38 \times A_V$. Reddening moves stars nearly along the YHK dwarf color sequence making it more difficult to distinguish unambiguously very low mass candidate brown dwarf objects from higher mass stars seen, e.g. through the galactic plane or towards star-forming regions. Other diagrams involving the Y-band may be somewhat more discriminating.

Subject headings: instrumentation: photometers – stars: general – stars: low-mass, brown dwarfs – ISM: extinction – infrared: stars

1. Introduction

The traditional near-infrared photometric bandpasses that are observable from the ground through windows of moderate atmospheric transparency are JHKLMNQ (and their slight variants K', Ks, L', M', N1, N2, N3, etc). This set of filters defined broadly as in Johnson (1966), with the H-band being devised soon thereafter by Becklin and similarly the Q-band by Low, neglected to include one rather clean window through the atmosphere near 1.035 μm . This region of the electromagnetic spectrum is in between the traditional “optical” and “infrared” wavelength regimes, which are usually divided from one another based

on detector technology (nowadays CCDs vs InSb or HgCdTe arrays) around $1 \mu\text{m}$. We discuss in this paper a filter called “Y” that takes advantage of this window and has particular interest for studies of low-mass and extremely cool stars and substellar objects, i.e. brown dwarfs.

The Y filter bandpass was designed by S.E.P. and K.M. after visually inspecting the USAF’s LOWTRAN (Selby & McClatchey, 1975) atmospheric transmission curve and also referring to Manducca and Bell (1979). The half-power points of the filter were aimed at the 75% transmission points of the broad atmospheric absorption features near 0.955 and $1.112 \mu\text{m}$. The filters were manufactured by Barr Associates (Worcester, MA). We name the filter “Y” in publication as a compromise between its current discrepant designations (X and Z as described below). Further, we choose Y to distinguish this filter from z and Z filters in use which are quantitatively different.

Nearly identical Y filters reside in the Keck Near-InfraRed Camera (NIRC, where it is called “Z”) and the Palomar 60” cassegrain InfraRed Camera (P60/IRC, where it is called “X”), as well as in the Palomar 200” D-78 and D-80 cameras. At 77°K , the Keck/NIRC filter has $\lambda_c = 1.032 \mu\text{m}$ and $\delta\lambda_c = 0.157 \mu\text{m}$ with $>50\%$ transmission from $0.965 - 1.115 \mu\text{m}$ while the P60/IRC filter has $\lambda_c = 1.04 \mu\text{m}$ and $\delta\lambda_c = 0.15 \mu\text{m}$ with $>50\%$ transmission from $0.9540 - 1.1105 \mu\text{m}$. The two filter profiles are nearly identical in shape with the Keck/NIRC filter 3-5% less transmissive. It was found to be difficult to produce the specified filter with peak transmission much above 70%; transmission profiles are given in Table 1. In Figure 1, filter transmission curves for the P60/IRC filter set are shown relative to a model of the atmosphere above Mauna Kea, produced using the program IRTRANS4 as presented on the UKIRT worldwide web pages ¹ for an altitude of 4200 km assuming 1.2 mm precipitable water vapor and zenith pointing. The Y-band is a relatively clean atmospheric window, both in terms of molecular absorption (Figure 1) and in terms of O_2 and OH night sky emission lines which are insignificant in the Y-band compared to J-band and H-band. Thermal background at Y-band is also insignificant.

The only other filter located in this atmospheric window is, ironically, the F1042M medium/narrowband filter in WFPC-2 aboard HST which has $\lambda_c = 1.015 \mu\text{m}$ and $\delta\lambda_c = 0.03 \mu\text{m}$. Since the original preparation of this manuscript we have also become aware of the UFTI “Z” filter as described in Leggett et al. (2002). This filter has half-power points at 0.851 and $1.056 \mu\text{m}$ (their Table 2), slightly blueward of and broader than our Y filter, and inclusive of the strong and broad atmospheric water absorption around $0.93 \mu\text{m}$ (see Figure 1). The optical “Gunn z ” and its successor the “Sloan z ” filters (Fukugita et al. 1996) as well as the “Bessel z ”, by contrast, are defined as long-pass filters and hence have their effective profiles determined by a rapidly falling CCD response curve towards $1 \mu\text{m}$ (Figure 1). The effective bandpass of these optical z filters is centered near 9250 \AA but can vary substantially from instrument to instrument depending on the CCD (e.g. SITe detectors vs the new red-sensitive LBNL devices as compared in NOAO Newsletter 67, p. 3).

The Y filter introduced here has a well-defined bandpass, as opposed to the long-pass optical z filters, and takes advantage of the relatively clean atmospheric window centered near $1.035 \mu\text{m}$, in moderate contrast to the UFTI Z filter. Y-band photometry therefore should be relatively independent of the specific detector and relatively insensitive to site-to-site differences in the transparency vs wavelength and the night-to-night variability of water vapor at a given site.

The motivating forces behind the present study are the instrumental/atmospheric advantages of the $1.035 \mu\text{m}$ window just mentioned, combined with the peak brightness of cool and ultra-cool dwarfs slightly

¹<http://www.ukirt.jach.hawaii.edu/JACpublic/UKIRT/astrometry/calib/atmos-index.html>.

longward of $1\ \mu\text{m}$. As shown in Figure 2, wavelengths $\sim 1\ \mu\text{m}$ represent the absolute peak in the spectral energy distributions of low-mass stars with spectral types $\sim \text{M5}$, and a strong local peak for stars and young brown dwarfs with spectral types $> \text{L6}$ (Burrows et al. 2001). In these very late type dwarfs the atmospheric opacity redistributes flux far from expectations based on blackbody radiation (Marley et al., 1996). Bolometric corrections become *positive* in the near-infrared bands, and J-H and H-K colors become *bluer* with decreasing effective temperature (Burrows et al., 1997).

Our goal here is to investigate the behavior of near-infrared colors involving the Y-band as a function of spectral type, and to determine the slope of the interstellar reddening vector. Our specific interest is in assessing the utility of the Y-filter in studies of low-mass objects in star-forming regions.

2. Observations

Imaging observations were obtained by L.A.H. on the nights of 1999, July 30 and August 1 (UT) using the cassegrain InfraRed Camera (P60/IRC; Murphy et al. 1995) at the Palomar 60" telescope under photometric sky conditions. The instrument contains a 256×256 HgCdTe NICMOS-3 array with $40\ \mu\text{m}$ pixels and produces a final platescale of $0.62''/\text{pixel}$. Observations at Y (called "X" in P60/IRC), H, and K were obtained using a 9-point dither pattern centered on target with $10''$ separation between adjacent grid points.

Dwarf optical standard stars spanning a range of B-V color from -0.32 (spectral class O) to 2.2 (spectral type M6.5) were selected from Landolt (1992) and supplemented at the red end with late-type objects from Kirkpatrick, Henry, & McCarthy (1991), Tinney (1993), Kirkpatrick, Henry, & Simons (1995), Reid, Hawley, & Gizis (1995), Hawley, Gizis, & Reid (1996), Kirkpatrick et al. (1999, 2000), and Burgasser et al. (2002). The latest spectral type observed was L8V. Infrared standard stars used for calibration of the H- and K-bands were selected from Persson et al. (1998) and include both unreddened G-type stars and reddened objects of unknown spectral type. A set of 8 A0 stars was observed in order to define the instrumental offsets between the Y filter and the H and K filters. The star GSPC S813-D (Lasker et al., 1988) was used to map the atmospheric extinction curve at Y-band. Finally, a moderately reddened field ($A_V = 10\text{-}20$ mag) in the Ophiuchus dark cloud was selected from the large area survey of Barsony et al. (1997) in order to study the interstellar extinction curve at Y-band. On 2001, September 9, some additional data for this program was obtained using the same equipment, by A. Burgasser and M. Brown, focussing on T dwarfs.

Also, observations that pre-date those above were made of 6 late-M- and L-type dwarfs using the Keck I telescope and NIRC (Matthews & Soifer 1994) by L.A.H. and J. Carpenter on 1999 February 10 (UT). Details are given in Hillenbrand & Carpenter (2000). Data of relevance to the present discussion were taken using a 5-point dither pattern in the Y (called "Z" in Keck/NIRC) and K filters with appropriate flat-field and dark current calibration frames also obtained.

3. Data Reduction

Our data reduction steps were performed within IRAF and include the standard procedures of applying a linearity correction, masking bad pixels, flat-fielding for correction of sensitivity variations across the array, sky-subtracting, and, finally, mosaicking the dither pattern to produce a final image for photometry. We describe these steps in detail for the P60/IRC observations though the same basic procedures were followed

for the Keck/NIRC data.

Non-linearity of the detector array was assessed from a series of 2 to 20 second exposures of the back of the telescope’s primary mirror cover taken at the end of the observing run. A central section of the array (1/4 of the total area) that is relatively defect-free was used to measure ADU vs exposure time. The count rate became significantly non-linear above 36,000 ADU, but to be safe images with a maximum pixel value above 30,000 ADU were discarded.

Below 30,000 counts the response was almost, but not quite, linear. The advertised correction (on the Palomar 60” web-page) linearizes data according to:

$$xl = x + x^2 * 1.85 \times 10^{-6} * (1 + \delta/EXPTIME)$$

where xl represents linear ADU and x raw ADU. For our data, $\delta = 3.385$ for an array speed of 1000 msec and 2.6 for a speed of 743 msec; hence integration times shorter than 5 seconds were avoided during the observations (sometimes by slightly defocussing the telescope when the observing plan called for observations of bright (<7.5) stars and integrations longer than 10 seconds preferred. Different linearization factors were examined and the correction with the lowest chi-squared relative to a linear curve was

$$xl = x + x^2 * 2.1 \times 10^{-6}$$

without a dependence on integration time for $EXPTIME > 5$ seconds. Both the magnitude of this correction and its difference from the standard correction given above are quite small.

Raw bias and flatfield frames were used to verify that the gain and readnoise of the detector were similar to the values in Murphy et al. (gain = $8e^-$; readnoise = $30e^-$). Bias frames were acquired as 1.365 second exposures with the filter wheel in the closed position. Ten frames were averaged after rejecting among the frames the highest and lowest value for each pixel. On each night a sequence of twilight exposures through each filter was used to construct flat field images. The minimum and maximum values for each pixel were rejected and the individual frames averaged after subtracting the bias image. The sky flat was then normalized to have an overall average value equal to unity. A bad pixel list was created based on a histogram of the normalized flatfield images by flagging all pixels below 0.65 and above 1.2. This list had considerable overlap with the advertised bad pixel list and the two lists were merged into a single bad pixel mask.

The images of astronomical targets were processed first by constructing sky images as averages of the 9 data frames in each dither sequence and subtracting this sky image from each individual data frame, then by determining the relative offsets in fractional pixels between each component of the dither pattern for the point source, and finally by applying the offsets and combining the individual frames with bad pixel masking into a mosaic. These steps were performed in the NOAO/IRAF environment.

4. Photometry and Calibration

We performed aperture photometry with the IRAF/PHOT task. An aperture radius of 12 pixels (15” diameter on the sky) was chosen uniformly for all objects after looking at FWHM values (2-4) pixels and nearest neighbor distances for the entire dataset. The bright A0 stars which tended to be in crowded fields due to proximity to the galactic plane, set the maximum aperture size. A growth curve of magnitude vs aperture size peaked in the range 11-14 pixels, beyond which the photometric errors increased substantially

as the magnitudes decreased for a sky annulus defined from 20-25 pixels. Only for a few (1-2) stars with FWHM just slightly less than 4 pixels (2.5") were the fluxes possibly under-estimated using an aperture only ~ 3 times their FWHM. The empirical aperture correction for these objects was difficult to find in many cases, but it was examined for several of the largest objects and found to be ~ 0.007 mag. Due to the difficulty in determining this number and its relatively small magnitude this correction was not applied. Uncertainty in the derived instrumental magnitudes was underestimated by IRAF/PHOT. A better estimate was obtained by examining the photometry of sources in the individual unmosaicked frames where the statistical scatter was observed to be ~ 0.01 mag. We therefore assumed a minimum photometric error of 0.01 mag and characterized our instrumental error as $\text{error}_{\text{IRAF/PHOT}} + 0.01$ mag.

The relationship between airmass and (standard - instrumental) magnitude was used to derive the zeropoints and atmospheric extinction curves for the K and H filters (Figure 3). Persson et al. (1998) standard stars that were observed over the airmass range 1.0-2.5, with airmass taken from the middle frame in the 9-position dither pattern, defined these relationships. The star GSPC S813-D was observed at 5-6 different airmasses each night for the explicit purpose of deriving the atmospheric extinction curve for the Y filter without having to know the standard star magnitudes at Y (Figure 4). Because conditions were photometric, data from both nights were combined in order to obtain a more tightly constrained fit. We now describe the fitting procedure.

While the slopes from each of the two nights were approximately the same at Y, H, and K, the zero point for the second night was systematically higher by a few hundredth's of a magnitude at all wavelengths. In combining data from the two nights, various vertical offsets of night 2 data to night 1 data were applied and the value which minimized the χ^2 in the linear fit of the extinction curve was retained. The linear fits assumed errors in airmass given by the 1/2 width of the airmass range of the observations, and errors in the ordinate given by a quadratic sum of our photometry errors ($\text{error}_{\text{IRAF/PHOT}} + 0.01$ mag) plus an arbitrarily assumed 0.01 mag error in the standard star magnitudes.

We thus calibrated the K and H photometry according to:

$$K_{\text{true}} = K_{\text{instr.}} - (0.065 \pm 0.010) \times AM_K + \begin{Bmatrix} 20.354 \pm 0.015(n1) \\ 20.389 \pm 0.015(n2) \end{Bmatrix}$$

$$H_{\text{true}} = H_{\text{instr.}} - (0.029 \pm 0.010) \times AM_H + \begin{Bmatrix} 20.925 \pm 0.015(n1) \\ 20.948 \pm 0.015(n2) \end{Bmatrix}$$

as shown in Figure 3. The second term in each equation contains a numerical value and error for the atmospheric extinction, $\kappa_{K,H}$, and the third term values and errors for the zero point, $ZP_{K,H}$. The extinction coefficients we derive for Palomar, $\kappa_K = 0.065$ and $\kappa_H = 0.029$ agree well with those from the 2MASS survey² at Mt. Hopkins a few hundred miles away and a few thousand feet higher, $\kappa_{K_s} = 0.061$ and $\kappa_H = 0.031$. Note that our quoted zero points are for A.M.=0, i.e. outside the atmosphere, assuming linear extrapolation of the fit derived from A.M.>1; see Figure 3 of Tokunaga, Simons, & Vacca (2002) for the (in)appropriateness of this extrapolation in various near-infrared bandpasses.

To calibrate the Y filter we assume by definition that unreddened A0 stars have zero color. The A0 stars observed for this program are lightly reddened due to the requirement that they be faint enough to observe with P60/IRC (implying $K > 7.5$ mag) which is essentially a minimum distance requirement given the

²http://www.ipac.caltech.edu/2mass/releases/first/doc/sec4_8.html

absolute magnitude of an A0 star, and hence a minimum reddening requirement given the properties of the local interstellar medium. We therefore include an interstellar extinction term in our calibration equations. We used both the K-band and the H-band data independently to derive the zeropoint at Y, from:

$$-K_{instr.} + Y_{instr.} = ZP_K - ZP_Y - (\kappa_K - \kappa_Y) \times AM - (A_K/A_V - A_Y/A_V) \times A_V$$

and a similar equation extrapolating to the Y-band from H-band instead of K-band, with the difference between the two approaches being less than 0.015 mag and within the $\sim 1\sigma$ A0 star photometry errors. $Y_{instr.}$ is the instrumental magnitude, ZP_Y is the zero point, κ_Y is the slope of the atmospheric extinction curve, and A_Y is the interstellar extinction. To find κ_Y we combined the data for GSPC S813-D from both nights, shifting the night 2 data by 0.035 mag to obtain the best fit to a straight line, giving $\kappa_Y = 0.047$. Figure 4 shows this slope determination. For the interstellar extinction term we use literature or Tycho B-V photometry and assume $A_V = 3.1 \times E(B-V)$, $A_Y = 0.38 \times A_V$ (anticipating our derivation of this result below in section 5.2), and $A_H = 0.155 \times A_V$, and $A_K = 0.090 \times A_V$ (Cohen et al., 1981). The two A0 stars with less well-determined B-V photometry (see Table 2) were left out of the final analysis since they introduced larger scatter and a systematic shift in the results between the H and K derivations.

With κ_Y and A_Y in hand, the above equation and an analogous one for H are solved for ZP_Y ; errors are calculated by summing in quadrature the errors from each term of the equations. From this solution for ZP_Y we then correct the 10-12 data points for GSPC S813-D and combine these measurements with the A0 points to derive the final Y-band calibration equation:

$$Y_{true} = Y_{instr.} - (0.047 \pm 0.018) \times AM_Y + \left\{ \begin{array}{l} 20.835 \pm 0.030(n1) \\ 20.875 \pm 0.030(n2) \end{array} \right\}.$$

Although the errors in the final K-band transformations are lower than those in the final H-band transformations, the zero point at Y derived from K and from H agree to well within the estimated errors, differing only by 0.015 mag. The χ^2 values for the fits are 0.8 and 0.7 for the extrapolation from K and H, respectively, a little less than unity which indicates a good assessment of errors. The difference in zero point between the two nights is 0.040 mag whereas we had shifted the data for S813-D between the two nights by 0.035 to derive the slope of atmospheric extinction, all consistent, and suggestive that only a single iteration of the procedure is needed.

The final Y, Y-H, and Y-K photometry for all objects is presented in Table 2 along with errors and ancillary information. These measurements are in the natural system of the camera, which should be that defined by the Persson et al. (1998) standards set up in part using this same camera. Magnitude uncertainties are given by:

$$\sigma_{magnitude} = \sqrt{\sigma_{ZP}^2 + airmass^2 * \sigma_{\kappa}^2 + \sigma_{instrumental}^2}$$

which contains 1- σ error terms for the zero point, atmospheric extinction assuming no uncertainty in the recorded airmass, and instrumental errors, $\sigma_{instrumental} = (\sigma_{IRAF/PHOT} + 0.01 \text{ mag})$. Color errors are assumed to be the root-sum-square of the relevant magnitude errors which means that we are ignoring the effects of any correlated errors in our photometry. Multiple measurements of the same star were averaged, mostly occurring in the case of GSPC standards. Also given in Table 2 are optical photometry and spectral types from the literature, and 2MASS photometry from the Second Incremental Release for comparison with our H and K measurements.

5. Analysis

5.1. Colors

Color-color diagrams were made for different color combinations using the H and K results presented in this paper and B, V, and I photometry obtained from the literature where available. These plots were superposed on standard color-color lines (e.g. Bessell & Brett 1988 transformed to the CIT photometric system) and good agreement was seen between our H and K photometry and expected I-K and H-K colors. Moving now to the Y filter, Figure 5 shows the infrared Y-K color compared to optical B-V and V-I colors. These colors redden together with increasing spectral type to mid-M in the case of B-V and mid-L in the case of V-I, at which point the optical colors become saturated and/or turn bluer while the infrared color continues to grow redder. Note that optical colors are not available for all of the objects in Table 2, particularly the later type, redder stars and brown dwarfs.

Plots of Y-H versus H-K, Y-K versus H-K, and Y-H versus Y-K were then investigated, as seen in Figures 6 and 7. The range of spectral types extends from sdO through T5V with photometry for the T6.5V brown dwarf Gl229b (Matthews et al., 1996) shown for comparison. Gaps in the data around Y-K = 0.3 and 0.8 mag are due to the lack of F and K stars in our sample. These plots reveal a relatively tight relationship between the YHK colors as they grow redder together through spectral type \sim L6V. Beyond L6V the colors turn blueward and from L7V to at least T6.5V the colors are nearly degenerate with those of warmer L and M stars.

There are six objects in common between this study and that of Leggett et al. (2002): LHS 3003 (M7V), LHS 2924 (M9V), 2MASS J1439284+192915 (L1V), DENIS-P J0205.4-1159 (L7V), 2MASS 1632291+190441 (L8V), and SDSSp 015141.69+124429.6 (T1). Our Y-band magnitudes are 0.3-0.6 mag brighter than their UFTI Z magnitudes and our colors accordingly bluer for these objects, consistent with the nature of the filter center and width differences described in our introduction.

5.2. Extinction

In order to study the effects of interstellar extinction on colors involving the Y-band filter, a moderately reddened field towards the edge of the Ophiuchus dark cloud was observed. Eleven stars were identified in all three filter images, but only 7 were bright enough in Y to produce acceptable photometry. L 134 and L 547 from Persson et al. (1998) were also included in this analysis. The locations of these 9 stars in YHK color-color diagrams did not enable us to deduce the magnitude of the reddening vector, as they lay basically along an extrapolation of the color-color line defined by the dwarf stellar/sub-stellar sequence (see Figures 6 and 7).

In order to quantify how objects redden in Y-band relative to V-band we retrieved J, H, and K_s photometry for the 7 Ophiuchus and the 2 Persson “red objects” from the 2MASS survey’s Second Incremental Release. We then dereddened these 9 stars using the 2MASS J-H and H- K_s colors and the Cohen et al. (1981) interstellar extinction curve until they intersected the dwarf color sequence in a J-H vs H- K_s diagram over the color range corresponding to spectral types K7-M6. Fortunately these stars all appear to be reddened background stars and not young stellar objects associated with the Ophiuchus (and other, in the case of the Persson et al. “red stars”) clouds, although we can not prove this. If they were indeed located within clouds they would likely have circumstellar dust/gas and hence colors that reflect substantial near-infrared excess in addition to the effects of reddening, invalidating our approach. The estimated H-K and J-H color

excess due to interstellar reddening was converted to A_V .

We then employed our Y-K vs H-K diagram to experiment with different values of A_Y and find the value that best put the 9 reddened stars on the empirically defined color-color line. 2MASS gives only upper limits to the J magnitudes for 2 of the 9 stars, implying lower limit A_V 's derived from the J-H vs H-K_s diagram; these stars were given little weight in the A_Y determination. The relation $A_Y = (0.38 \pm 0.03) \times A_V$ was found to best bring the ensemble of stars onto the color sequence defined by unreddened stars. The derived value of total extinction at Y-band relative to V-band is within the rough expectations from interpolation between adjacent atmospheric windows, given $A_J = 0.265 \times A_V$ and $A_I = 0.617 \times A_V$. For comparison, $A_{z(gunn)} = 0.472 \times A_V$ and $A_{z(sloan)} = 0.453 \times A_V$ have been quoted in the literature (Schlegel et al. 1998). No information is available to the authors regarding $A_{Z(UFTI)}$.

6. Discussion

Soon after incorporation of the H-band into standard filter sets it was shown by Bahng (1969) that the colors of GKM stars differ from blackbody expectations in the near-infrared. The excursions from monotonic reddening with advancing spectral type are largely due to the influence of H- opacity in the H-band. Deviation from blackbody colors is apparent in the now-familiar J-H vs H-K diagram in the growth of J-H relative to H-K in a manner that is “faster” than blackbody from spectral types G through K, and then in the peak and blueward turnover of J-H near spectral type K7 as H-K continues slowly to get redder. After spectral type M4, J-H again grows redder with increasing H-K through \sim L6.

In our data we see that colors involving Y also steadily redden out to Y-J \approx 1 mag, Y-H \approx 2.5 mag, and Y-K \approx 3 mag at spectral type L6V. Then, Y-H and Y-K colors both turn sharply blueward in the L6-L8V temperature range with later T-type objects having colors similar to those of warmer L and M stars. Y-J colors turn only softly blueward, remaining relatively constant from L6-T4V and then overlapping dwarf stars only as warm as M8-M9 by spectral type T5V.

Cool M- and L-type objects initially become redder with advancing spectral type because of increased opacity sources at the shorter Y-band, mostly H₂O absorption at first, then H₂-H₂ collision induced absorption. When CH₄ opacity begins to contribute substantially in the T dwarfs, the H and K fluxes decrease, sending the colors bluer. This bluing behavior is consistent with that exhibited in J-H vs H-K diagrams of late-type objects (e.g. Burgasser et al. 2002) where the transition between L-dwarfs and T-dwarfs takes colors from the reddest occupied by stars, all the way through the heart of the color-color diagram past every known astronomical object, to the bluest colors occupied by both hot stars and cool brown dwarfs. In the case of YHK colors, however, instead of crossing the entire color sequence the T dwarf sequence overlaps the only slightly warmer L and M dwarfs (see Figures 6 and 7). The latest T dwarfs ($>$ T5) appear to fall more blueward in Y-K than Y-H and hence still may be uniquely distinguishable in this color-color plane. Overall, Y-J appears to be the most robust diagnostic of late-type cool stars and brown dwarfs.

The sharp turnaround in Y-K and Y-H occurring in the T dwarfs stands in contrast to T dwarf colors at longer and shorter wavelengths. K-L' colors appear to redden out to at least L7, become flat with advancing spectral type from L7 to T1, and then redden again from T1 to at least T6 (Stephens et al., 2001; Leggett et al. 2002). However, hampering the utility of this color diagnostic is that L-band data on stellar/sub-stellar photospheres is hard to come by due to high thermal backgrounds and resulting low sensitivity. I-z colors have been studied through only the L spectral types, with Steele & Howells (2000) claiming that I-z colors redden through the M and early L range, flatten from L1-L5, and then redden again towards even later

spectral types. However, I-band photometry is not readily obtainable for many of the nearby L and T objects due to source faintness ($M_I = 15$ mag at M9 but >18 mag by L7). We thus advocate the use of Y-K, Y-H, and Y-J colors for identifying very cool objects.

The downside of the Y-K vs Y-H diagram is the effect of extinction, which drives stars nearly directly along the dwarf locus. In other color-color planes such as I-Y or Y-J vs Y-K and J-K, however, there is more leverage of extinction vs the stellar/substellar color sequence.

7. Conclusions

We present the first exploration of the colors of normal dwarf stars (and some brown dwarfs) spanning spectral types sdO through T5V using the Y-band at $1.035 \mu\text{m}$. The behavior of the earth’s atmosphere is relatively clean in this window of near unit transparency and few emission lines, especially compared to the other near-infrared J, H, and K windows. Atmospheric extinction at Y-band is <0.05 mag per airmass. The relationship between interstellar extinction in the Y-band and that at V-band is $A_Y = (0.38 \pm 0.03) \times A_V$.

Our photometric results, including errors, appear in Table 2. Although for most objects only one measurement was taken, photometric variability should not be an issue since our stars are mostly accepted photometric standards in either the optical or the near-infrared. The exception to this are the late type dwarfs (late M, L, and T spectral types) for which small-amplitude near-infrared variability has been reported in some objects (e.g. Bailer-Jones & Mundt, 2001).

The large range in color exhibited by low-mass stars and brown dwarfs makes colors involving the Y-band particularly diagnostic of these extremely cool objects. The I-Y, Y-J, Y-H, and Y-K colors all grow redder with increasing spectral type through at least L6V. At later spectral types YJHK colors all saturate and turn blueward to somewhat differing degrees, due to the strong peak in the SEDs of extremely cool objects in the $1.1\text{-}1.3 \mu\text{m}$ region. This bluing is caused by H_2O , CH_4 , and collision-induced H_2 opacity suppressing first the K-band and then the H-band flux as temperatures grow cooler (e.g. Marley et al. 2002). Infrared spectroscopy of G1229b and G1570d, the coolest known T dwarfs, appear to confirm these statements for most of the T spectral type range. Colors involving the Y, J, H, and M bands can uniquely identify extremely cool brown dwarfs and so-called “planetary mass objects” apart from other astronomical targets, and should form the basis for deep surveys of field and cluster samples in the future.

We acknowledge with appreciation Adam Burgasser for obtaining P60/IRC (“X”) Y-band data for us of several T-dwarfs. LAH thanks John Carpenter for allowing her to talk him into observing with the Keck/NIRC (“Z”) Y-band filter during data acquisition for our H/K study of Orion Nebula Cluster faint stars and brown dwarfs. This publication makes use of data products from the Two Micron All Sky Survey (2MASS) and has benefited from information provided by the SIMBAD database.

REFERENCES

- Bahng, J. 1969, MNRAS 143, 73
 Bailer-Jones, C.A.L. & Mundt, R. 2001, AA 367, 218
 Barsony, M., Kenyon, S.J., Lada, E.A., & Teuben, P.J., 1997 ApJS 112, 109
 Bessell, M.S. & Brett, J.M. 1988, PASP 100, 1134

- Burgasser, A.J., Kirkpatrick, J.D., Brown, M.E., Reid, I.N., Burrows, A., Liebert, J., Matthews, K., Gizis, J.E., Dahn, C.C., Monet, D.G., Cutri, R.M., & Skrutskie, M.F. 2002, *ApJ* 564, 421
- Burrows, A., Hubbard, W.B., Lunine, J.I., & Liebert, J. 2001, *Rev. Mod. Phys.*, in press.
- Burrows, A., Marley, M., Hubbard, W.B., Lunine, J.I., Guillot, T., Saumon, D., Freedman, R., Sudarsky, D., & Sharp, C. 1997, *ApJ* 491, 856
- Cohen, J.G., Persson, S.E., Elias, J.H., & Frogel, J.A. 1981, *ApJ* 249, 481
- Fukugita, M., Ichikawa, T., Gunn, J.E., Doi, M., Shimasaku, K., Schneider, D.P. 1996 *AJ* 111, 1748
- Geballe, T.R., Knapp, G.R., Leggett, S.K., Fan, X., et al 2002, *ApJ* 564, 466
- Hawarden, T.G., Leggett, S.K., Letawsky, M.B., Ballantyne, D.R., & Casali, M.M. 2001, *MNRAS*, 325, 563
- Hawley, S.L., Gizis, J.E., & Reid, I.N. 1996, *AJ* 112, 2799
- Hillenbrand, L.A. & Carpenter, J.M. 2000, *ApJ* 540, 236
- Johnson, H.L. 1966, *ARAA* 4, 193
- Kirkpatrick, J.D., Henry, T.J., & McCarthy, D.W. 1991, *ApJS* 77, 417
- Kirkpatrick, J.D., Henry, T.J., & Simons, D.A. 1995, *AJ* 109, 797
- Kirkpatrick, J.D., Reid I.N., Liebert J., Cutri R.M., Nelson B., Beichman C.A., Dahn C.C., Monet D.G., Gizis J.E., Skrutskie M.F. 1999, *ApJ* 519, 802
- Kirkpatrick, J.D., Reid, I.N., Liebert, J., Gizis, J.E., Burgasser, A.J., Monet, D.G., Dahn, C.C., Nelson, B., & Williams, R.J, 2000, *AJ* 120, 447
- Landolt, A.U. 1992, *AJ* 104, 340
- Lasker, B.M., Sturch, C.R., Lopez, C., Mallama, A.D., et al., 1988, *ApJS* 68, 1
- Leggett, S.K. 1992, *ApJS* 82, 351
- Leggett, S.K., Allard, F., & Hauschildt, P.H. 1998, *ApJ* 509, 836
- Leggett, S.K., Allard, F., Dahn, C., Hauschildt, P. H., Kerr, T. H., & Rayner, J. 2000a *ApJ* 535, 965
- Leggett, S.K., Geballe, T.R., Fan, X., Schneider, D.P., et al. 2000b *ApJL* 536, 35
- Leggett, S.K., Golimowski, D.A., Fan, X., Geballe, T.R., et al. 2002, *ApJ* 564, 452
- Manduca, A. & Bell, R.A. 1979, *PASP* 91, 848
- Marley, M.S., Saumon, D., Guillot, T., Freedman, R.S., Hubbard, W.B., Burrows, A., & Lunine, J.I. 1996, *Science* 272, 1919
- Marley, M.S., Seager, S., Saumon, D., Lodders, K., Ackerman, A.S., & Freedman, R. 2002 *ApJ*, 568, 335
- Matthews, K., & Soifer, B. T. 1994, *Infrared Astronomy with Arrays: the Next Generation*, ed. I. McLean (Dordrecht: Kluwer), 239
- Matthews, K., Nakajima, T., Kulkarni, S.R., & Oppenheimer, B.R. 1996, *AJ* 112, 1678
- Murphy, D.C., Persson, S.E., Pahre, M.A., Sivaramakrishnan, A.,M. & Djorgovski, S.G. 1995, *PASP* 107, 1234
- Nakajima, T., Oppenheimer, B.R., Kulkarni, S.R., Golimowski, D.A., Matthews, K., & Durrance, S.T. 1995, *Nature* 378, 463
- Reid, I.N., Hawley, S.L., & Gizis, J.E. 1995, *AJ* 110, 1838

- Persson, E., Murphy, D.C., Krzeminski, W., Roth, M., & Rieke, M.J. 1998, AJ 116, 2475
- Schlegel, D.J., Finkbeiner, D.P., & Davis, M. 1998, ApJ 500, 525
- Selby, J.E.A. & McClatchey, R.A., “Atmospheric Transmittance From 0.25 to 28.5 μm : Computer Code LOWTRAN 3,” Air Force Cambridge Research Laboratories, 7 May 1975
- Steele, I.A., & Howells, L. 2000, MNRAS 313, L43
- Stephens, D.C., Marley, M.S., Noll, K.S., & Chanover, N. 2001, ApJL 556, 97
- Tinney, C.G. 1993, ApJ 414, 279
- Tokunaga, A.T., Simons, D.A., & Vacca, W.D. 2002, PASP 114, 180

Table 1. **Y-Band Filter Transmission**

Wavelength [\AA]	Transmission (P60/IRC)	Transmission (Keck/NIRC)
9260.	0.0000	0.0000
9270.	0.0016	0.0000
9280.	0.0032	0.0000
9290.	0.0044	0.0000
9300.	0.0050	0.0000
9310.	0.0060	0.0000
9320.	0.0070	0.0010
9330.	0.0080	0.0014
9340.	0.0100	0.0024
9350.	0.0130	0.0026
9360.	0.0160	0.0037
9370.	0.0180	0.0051
9380.	0.0200	0.0059
9390.	0.0250	0.0078
9400.	0.0300	0.0097
9410.	0.0350	0.0117
9420.	0.0400	0.0140
9430.	0.0500	0.0170
9440.	0.0600	0.0211
9450.	0.0700	0.0259
9460.	0.0800	0.0300
9470.	0.1100	0.0365
9480.	0.1300	0.0462
9490.	0.1633	0.0542
9500.	0.2000	0.0618
9510.	0.2315	0.0758
9520.	0.2530	0.0847
9530.	0.2730	0.1082
9540.	0.3000	0.1264
9550.	0.3401	0.1505
9560.	0.3903	0.1716
9570.	0.4454	0.1944
9580.	0.5000	0.2192
9590.	0.5497	0.2539
9600.	0.5933	0.2948
9610.	0.6302	0.3248
9620.	0.6600	0.3938

Table 1—Continued

Wavelength [\AA]	Transmission (P60/IRC)	Transmission (Keck/NIRC)
9630.	0.6826	0.4533
9640.	0.6991	0.4982
9650.	0.7111	0.5455
9660.	0.7200	0.5871
9670.	0.7271	0.6177
9680.	0.7328	0.6435
9690.	0.7371	0.6621
9700.	0.7400	0.6748
9710.	0.7417	0.6864
9720.	0.7427	0.6976
9730.	0.7436	0.6999
9740.	0.7450	0.7057
9750.	0.7472	0.7090
9760.	0.7500	0.7109
9770.	0.7528	0.7124
9780.	0.7550	0.7136
9790.	0.7563	0.7151
9800.	0.7566	0.7152
9810.	0.7561	0.7165
9820.	0.7550	0.7165
9830.	0.7533	0.7165
9840.	0.7511	0.7165
9850.	0.7484	0.7165
9860.	0.7450	0.7134
9870.	0.7411	0.7125
9880.	0.7369	0.7110
9890.	0.7331	0.7083
9900.	0.7300	0.7058
9910.	0.7280	0.7019
9920.	0.7267	0.6993
9930.	0.7259	0.6964
9940.	0.7250	0.6935
9950.	0.7238	0.6891
9960.	0.7225	0.6841
9970.	0.7212	0.6816
9980.	0.7200	0.6770
9990.	0.7191	0.6739

Table 1—Continued

Wavelength [\AA]	Transmission (P60/IRC)	Transmission (Keck/NIRC)
10000.	0.7183	0.6708
10010.	0.7170	0.6655
10020.	0.7150	0.6628
10030.	0.7119	0.6614
10040.	0.7081	0.6574
10050.	0.7039	0.6547
10060.	0.7000	0.6534
10070.	0.6966	0.6534
10080.	0.6939	0.6493
10090.	0.6917	0.6480
10100.	0.6900	0.6467
10110.	0.6888	0.6426
10120.	0.6878	0.6426
10130.	0.6866	0.6426
10140.	0.6850	0.6427
10150.	0.6827	0.6427
10160.	0.6801	0.6427
10170.	0.6774	0.6373
10180.	0.6750	0.6359
10190.	0.6732	0.6319
10200.	0.6719	0.6292
10210.	0.6709	0.6279
10220.	0.6700	0.6265
10230.	0.6690	0.6239
10240.	0.6678	0.6225
10250.	0.6665	0.6225
10260.	0.6650	0.6225
10270.	0.6634	0.6212
10280.	0.6619	0.6198
10290.	0.6607	0.6172
10300.	0.6600	0.6172
10310.	0.6599	0.6145
10320.	0.6604	0.6131
10330.	0.6612	0.6105
10340.	0.6620	0.6105
10350.	0.6628	0.6091
10360.	0.6635	0.6091

Table 1—Continued

Wavelength [\AA]	Transmission (P60/IRC)	Transmission (Keck/NIRC)
10370.	0.6642	0.6078
10380.	0.6650	0.6078
10390.	0.6659	0.6092
10400.	0.6671	0.6092
10410.	0.6684	0.6078
10420.	0.6700	0.6092
10430.	0.6718	0.6092
10440.	0.6735	0.6092
10450.	0.6747	0.6092
10460.	0.6750	0.6105
10470.	0.6743	0.6119
10480.	0.6728	0.6119
10490.	0.6712	0.6146
10500.	0.6700	0.6146
10510.	0.6696	0.6146
10520.	0.6697	0.6133
10530.	0.6699	0.6133
10540.	0.6700	0.6146
10550.	0.6695	0.6146
10560.	0.6685	0.6133
10570.	0.6670	0.6133
10580.	0.6650	0.6120
10590.	0.6627	0.6093
10600.	0.6601	0.6079
10610.	0.6575	0.6066
10620.	0.6550	0.6026
10630.	0.6527	0.6026
10640.	0.6504	0.5999
10650.	0.6479	0.5972
10660.	0.6450	0.5959
10670.	0.6415	0.5945
10680.	0.6375	0.5945
10690.	0.6336	0.5892
10700.	0.6300	0.5865
10710.	0.6270	0.5865
10720.	0.6244	0.5865
10730.	0.6222	0.5838

Table 1—Continued

Wavelength [\AA]	Transmission (P60/IRC)	Transmission (Keck/NIRC)
10740.	0.6200	0.5798
10750.	0.6178	0.5757
10760.	0.6154	0.5744
10770.	0.6129	0.5690
10780.	0.6100	0.5636
10790.	0.6068	0.5623
10800.	0.6032	0.5582
10810.	0.5993	0.5569
10820.	0.5950	0.5542
10830.	0.5905	0.5529
10840.	0.5861	0.5435
10850.	0.5825	0.5408
10860.	0.5800	0.5408
10870.	0.5790	0.5367
10880.	0.5785	0.5341
10890.	0.5775	0.5260
10900.	0.5750	0.5233
10910.	0.5701	0.5193
10920.	0.5636	0.5166
10930.	0.5565	0.5139
10940.	0.5500	0.5072
10950.	0.5448	0.5004
10960.	0.5408	0.4991
10970.	0.5377	0.4924
10980.	0.5350	0.4910
10990.	0.5326	0.4870
11000.	0.5306	0.4843
11010.	0.5296	0.4803
11020.	0.5300	0.4776
11030.	0.5318	0.4736
11040.	0.5335	0.4736
11050.	0.5335	0.4695
11060.	0.5300	0.4668
11070.	0.5213	0.4669
11080.	0.5059	0.4669
11090.	0.4826	0.4642
11100.	0.4500	0.4628

Table 1—Continued

Wavelength [\AA]	Transmission (P60/IRC)	Transmission (Keck/NIRC)
11110.	0.4075	0.4588
11120.	0.3577	0.4480
11130.	0.3041	0.4426
11140.	0.2500	0.4292
11150.	0.1986	0.3942
11160.	0.1519	0.3713
11170.	0.1118	0.3349
11180.	0.0800	0.3147
11190.	0.0578	0.3038
11200.	0.0435	0.2929
11210.	0.0350	0.2819
11220.	0.0300	0.2710
11230.	0.0266	0.2601
11240.	0.0242	0.2492
11250.	0.0221	0.2383
11260.	0.0200	0.2274
11270.	0.0176	0.2164
11280.	0.0149	0.2055
11290.	0.0123	0.1946
11300.	0.0100	0.1837
11310.	0.0082	0.1728
11320.	0.0069	0.1618
11330.	0.0059	0.1509
11340.	0.0050	0.1400
11350.	0.0042	0.1291
11360.	0.0034	0.1182
11370.	0.0027	0.1072
11380.	0.0020	0.0963
11390.	0.0014	0.0854
11400.	0.0008	0.0745
11410.	0.0004	0.0636
11420.	0.0000	0.0527
11430.	0.0000	0.0417
11440.	0.0000	0.0308
11450.	0.0000	0.0199
11460.	0.0000	0.0090
11470.	0.0000	0.0000

Table 1—Continued

Wavelength [\AA]	Transmission (P60/IRC)	Transmission (Keck/NIRC)
-----------------------------	------------------------	--------------------------

Table 2. Photometry of Optical/Infrared Standard Stars and Additional Red Objects¹

Source Name	SpT	B-V [mag]	V-I [mag]	I-K [mag]	Y [mag]	Y err. [mag]	Y-H [mag]	Y-H err. [mag]	Y-K [mag]	Y-K err. [mag]	J _{2MASS} [mag]	H _{2MASS} [mag]	K _{2MASS} [mag]	Comment
PG 2213-006	sdO	-0.217	-0.203	-0.378	14.559	0.030	-0.132	0.048	-0.167	0.108	14.70	14.78	14.60	Landolt
HD 218902	A0V	-0.01	-	-	10.244	0.036	-0.011	0.045	-0.020	0.046	10.23	10.22	10.20	zero point
HD 222644	A0/A1V	0.1:	-	-	10.571	0.032	0.010	0.040	-0.004	0.040	10.56	10.54	10.54	zero point
SA 112-805	A0/A1	0.152	0.138	0.205	11.836	0.030	0.051	0.038	0.065	0.041	-	-	-	Landolt / zero point
HD 191398	A0V	0.09	-	-	8.739	0.026	0.084	0.033	0.094	0.033	8.67	8.60	8.61	zero point
HD 228700	A0V	0.11	-	-	8.905	0.026	0.119	0.033	0.126	0.034	9.392	9.33	9.31	zero point
HD 161481	A0	0.24	-	-	8.594	0.029	0.157	0.036	0.156	0.037	-	-	-	zero point
HD 161168	A0	0.3:	-	-	8.856	0.038	0.109	0.047	0.163	0.048	8.81	8.77	8.70	zero point
SA 109-71	A0	0.323	0.41	0.496	10.823	0.035	0.170	0.044	0.206	0.045	-	-	-	Landolt / zero point
HD 167163	A0V	0.35	-	-	8.705	0.029	0.179	0.037	0.222	0.037	-	-	-	zero point
SA 115-420	F5	0.468	0.58	0.657	10.362	0.027	0.392	0.035	0.399	0.036	-	-	-	Landolt
GSPC P576-F = SJ 9183	G	-	-	-	12.296	0.030	-	-	0.419	-	-	-	-	Persson
GSPC P550-C = SJ 9143 ³	G	-	-	-	12.610	0.05	0.493	0.05	0.542	0.05	-	-	-	Persson
SA 113-492	G0:	0.553	0.684	0.785	11.279	0.028	0.545	0.036	0.546	0.038	-	-	-	Landolt
GSPC P290-D = SJ 9188	G	-	-	-	11.875	0.026	0.524	0.034	0.581	0.036	-	-	-	Persson
GSPC P330-E = SJ 9166	G	-	-	-	12.041	0.018	0.565	0.022	0.582	0.023	11.79	11.46	11.43	Persson
FS 35	K0	0.8:	-	-	12.359	0.030	0.52 ⁵	0.030	0.582	0.030	12.20 ⁴	11.83 ⁴	11.75	Hawarden
GSPC S813-D = SJ 9182	G	-	-	-	11.697	0.009	0.552	0.010	0.586	0.010	11.47	11.12	11.13	Persson
GSPC P545-C = SJ 9134 ³	G	-	-	-	12.155	0.05	0.531	0.05	0.598	0.05	-	-	-	Persson
GSPC P182-E = SJ 9177	G	-	-	-	12.328	0.016	0.558	0.020	0.603	0.021	12.09	11.76	11.71	Persson
SA 113-493	G5:	0.786	0.824	0.97	10.666	0.028	0.608	0.036	0.664	0.037	-	-	-	Landolt
SA 109-949	G8:	0.806	1.02	1.130	11.384	0.029	0.595	0.037	0.668	0.038	-	-	-	Landolt
GSPC S867-V = SJ 9155 ³	G5	0.68	-	-	12.363	0.05	0.719	0.05	0.729	0.05	11.98 ⁴	11.64 ⁴	11.59 ⁴	Persson / Hawarden
2MASS J2254188+312349	T5V	-	-	-	16.037	0.051	1.00 ⁵	0.051	0.823	0.092	15.28	15.04	14.83	late-type
Gl 229b ²	T6.5V	-	-	>5.6	15.3	-	1.0	-	0.9	-	-	-	-	late-type
SA 113-495	G:	0.947	1.01	1.306	11.055	0.028	0.849	0.036	0.906	0.037	-	-	-	Landolt
SA 110-477	-	1.345	1.707	1.685	11.572	0.036	0.823	0.045	0.947	0.046	-	-	-	Landolt
SA 109-956	-	1.283	1.525	1.796	12.516	0.029	1.038	0.038	1.160	0.041	-	-	-	Landolt
Gl 754.1B	M2.5V	1.469	2.87	1.475	8.547	0.037	0.964	0.045	1.193	0.045	9.54:	9.634	9.01:	late-type
SA 109-954	-	1.296	1.496	1.929	10.254	0.028	1.064	0.036	1.204	0.037	-	-	-	Landolt
LHS 3409 = GJ 4076	M3.5V-sdM4.5	1.85	2.66	2.223	11.486	0.027	0.964	0.034	1.211	0.035	10.98 ⁴	10.49 ⁴	10.26 ⁴	late-type
GJ 1220 = LHS 3297	M4V	1.73	2.96	2.489	10.128	0.032	1.083	0.040	1.339	0.040	-	-	-	late-type
GJ 1215 = LHS 3277	M5.5V	1.96	3.32	2.875	10.377	0.032	1.105	0.040	1.404	0.040	-	-	-	late-type
SA 110-364	-	1.133	1.281	1.996	11.775	0.035	1.120	0.043	1.409	0.044	-	-	-	Landolt
LHS 523 = GJ 4281	M6.5V	2.03	4.26	3.133	11.354	0.030	1.134	0.039	1.449	0.040	10.79 ⁴	10.22 ⁴	9.91 ⁴	late-type
BRI 2202-1119 = LP 759-25	M6.5V	-	-	2.936	12.226	0.032	1.158	0.040	1.464	0.040	11.68	11.06	10.73	late-type
TVLM 868-53850	M6:	-	-	-	12.195	0.031	1.197	0.039	1.504	0.040	11.53	10.94	10.65	Persson
VB 8	M7V	2.2	4.56	3.405	10.455	0.033	1.232	0.042	1.591	0.042	-	-	-	late-type
LHS 2632 = LP 321-222 ³	M7.5V	-	-	-	13.001	0.05	1.41 ⁵	0.05	1.77 ⁵	0.05	12.26	11.59	11.23	late-type
LHS 3003 = GJ 3877 ³	M7V	1.34	4.52	3.196	10.735	0.05	1.41 ⁵	0.05	1.815	0.05	9.96	9.32	8.92	late-type
2MASS J1524248+292535 ³	-	-	-	-	12.069	0.05	-	-	1.847	0.05	-	-	-	late-type
SDSSp 175032.96+175903.9	T3.5	-	-	-	17.427	0.132	1.49 ⁵	0.132	1.96 ⁵	0.132	16.32	15.94	15.47	late-type; z*=19.63
SDSSp 015141.69+124429.6	T1	-	-	-	17.173	0.111	1.63 ⁵	0.111	1.965	0.138	16.25	15.54	15.18	late-type; z*=19.51

Table 2—Continued

Source Name	SpT	B-V [mag]	V-I [mag]	I-K [mag]	Y [mag]	Y err. [mag]	Y-H [mag]	Y-H err. [mag]	Y-K [mag]	Y-K err. [mag]	J_{2MASS} [mag]	H_{2MASS} [mag]	K_{2MASS} [mag]	Comment
TVLM 868-110639	M9V	-	-	4.422	13.470	0.033	1.584	0.042	2.064	0.043	-	-	-	Persson
LHS 2924 = GJ 3849 ³	M9V	1.62:	4.37	4.446	12.940	0.05	1.77 ⁵	0.05	2.176	0.05	11.92 ⁴	11.17 ⁴	10.75 ⁴	late-type
2MASSW J1439284+192915 ³	L1V	-	4.92	4.53	13.778	0.05	1.73 ⁵	0.05	2.187	0.05	12.76	12.05	11.58	late-type
2MASSW J0030438+313932	L2V	-	-	-	16.448	0.033	1.864	0.047	2.418	0.078	15.49	14.58	13.99	late-type
DENIS-P J0205.4-1159	L7V	-	-	5.31	15.425	0.037	1.84 ⁵	0.037	2.437	0.042	14.58	13.59	12.98	late-type
2MASSW J2208136+292121	L2V	-	-	-	16.894	0.068	2.06 ⁵	0.068	2.826	0.076	15.82	14.83	14.09	late-type
2MASSW J1728114+394859	L7V	-	-	-	16.821	0.064	2.04 ⁵	0.064	2.92 ⁵	0.064	15.96	14.78	13.90	late-type
2MASSI J1029216+162652 ³	L2.5	-	-	-	15.565	0.05	2.22 ⁵	0.05	2.952	0.05	14.31	13.35	12.61	late-type
2MASSW J1632291+190441	L8V	-	-	-	16.984	0.043	2.260	0.059	2.993	0.081	15.86	14.59	13.98	late-type
2MASSI J0103320+193536	L6V	-	-	-	17.312	0.123	2.43 ⁵	0.123	3.169	0.127	16.26	14.88	14.15	late-type
L 134-5	-	-	-	-	12.976	0.033	3.296	0.041	4.012	0.041	-	-	-	Persson / extincted
“Oph2” = 2MASS J162705-242010	-	-	-	-	17.530	0.094	3.677	0.105	4.612	0.109	12.70	10.50	9.36	extincted
“Oph5” = 2MASS J162705-242036	-	-	-	-	14.813	0.038	3.724	0.047	4.668	0.047	-	14.47	12.97	extincted
L 547	-	-	-	-	13.750	0.030	3.833	0.037	4.741	0.037	10.83	10.39	10.25	Persson / extincted
“Oph9” = 2MASS J162703-241832	-	-	-	-	18.408	0.118	3.647	0.137	4.907	0.136	-	-	-	extincted
“Oph8” = 2MASS J162707-242009	-	-	-	-	14.582	0.038	4.117	0.046	5.186	0.046	-	-	-	extincted
“Oph6” = 2MASS J162706-241923	-	-	-	-	19.248	0.309	4.202	0.320	5.363	0.321	-	14.86	13.83	extincted
“Oph11” = 2MASS J162658-241837	-	-	-	-	18.758	0.167	4.120	0.179	5.363	0.179	-	14.51	13.34	extincted
“Oph3” = 2MASS J162702-242040	-	-	-	-	17.519	0.111	4.518	0.117	5.883	0.117	-	-	-	extincted

¹ Table is sorted by Y-K color. Spectral types and luminosity classes are given where available and taken, along with B-V and V-I photometry from the literature. I-K colors are calculated by combining literature I with the present K measurements. Y, Y-H, and Y-K photometry is newly measured here. Errors include terms for zero point, atmospheric extinction, and photon statistics added in quadrature. J_{2MASS} , H_{2MASS} , and K_{2MASS} values come from 2MASS’ Second Incremental Release and have errors typically 0.03 - 0.04 mag. Comment indicates the type of object, either a photometric standard star from Landolt (1992), Persson (1998), or Hawarden (2001), a later type usually spectroscopic standard star, or an extincted/reddened object.

² Gl 229b photometry is from Nakajima et al. 1995 and Matthews et al., 1996.

³ YHK data is from Keck/NIRC instead of P60/IRC.

⁴ Star’s JHK photometry is from Geballe et al 2002, Hawarden et al. 2001, Leggett et al. 1998, or Leggett 1992 (largely in MKO/UKIRT system) instead of from 2MASS.

⁵ Star’s quoted Y-H or Y-K color is from measured Y magnitude and 2MASS or other H,K/ K_s photometry.

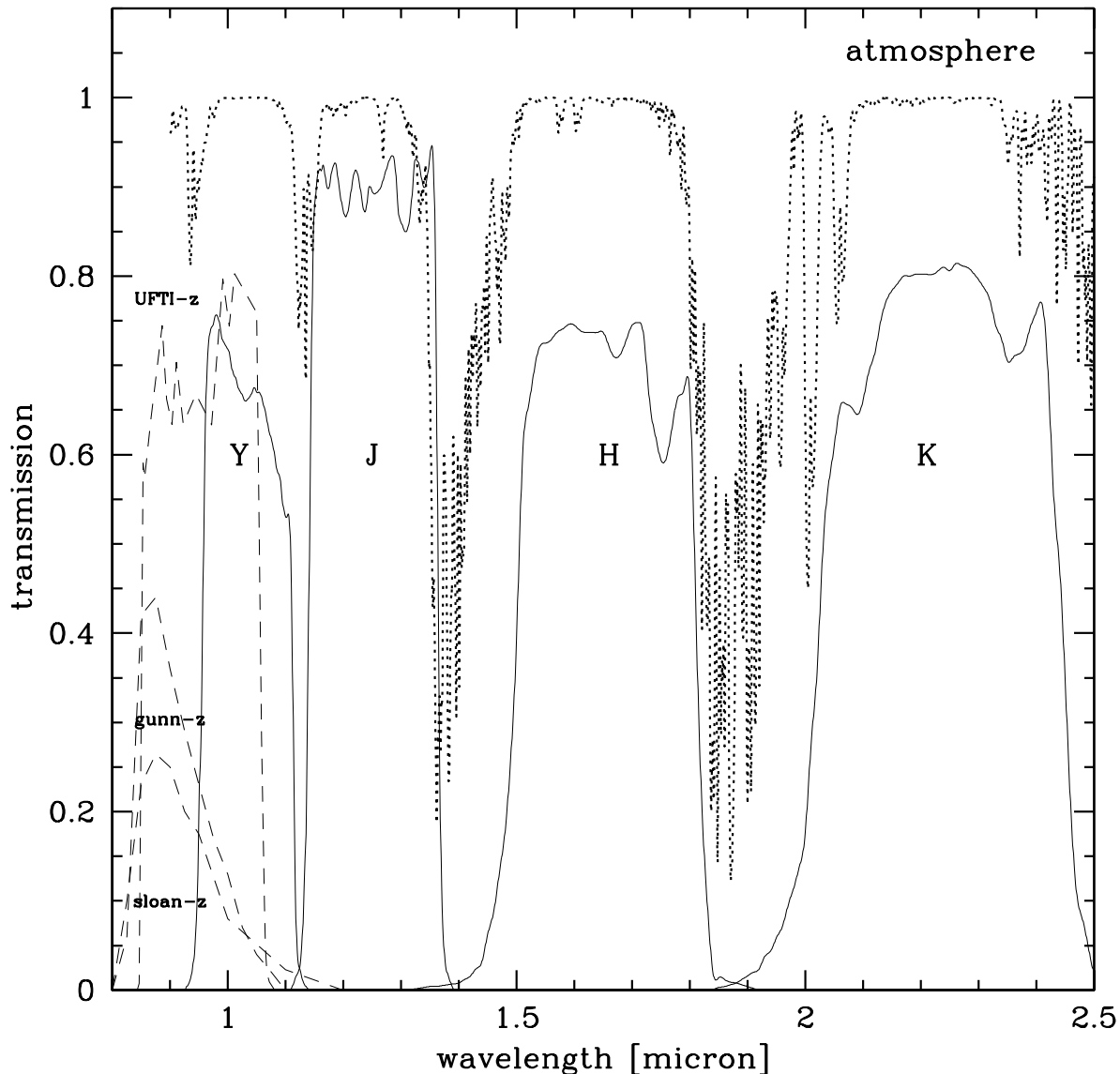


Fig. 1.— Near-infrared Y, J, H, and K filter transmission profiles (solid lines) for the Palomar 60" cassegrain infrared camera (P60/IRC) filters at 77 K, superposed on atmospheric transmission at Mauna Kea (dotted line). Also shown for comparison to the Y-band filter are the optical Gunn-z and Sloan-z filter profiles convolved with typical CCD response and the UFTI-Z filter (cold and already convolved with the Mauna Kea atmospheric transmission as presented in Leggett et al, 2002). The near-infrared Y is longward of previously defined z and Z filters, and takes advantage of the relatively clean atmospheric window centered near 1.035 μm .

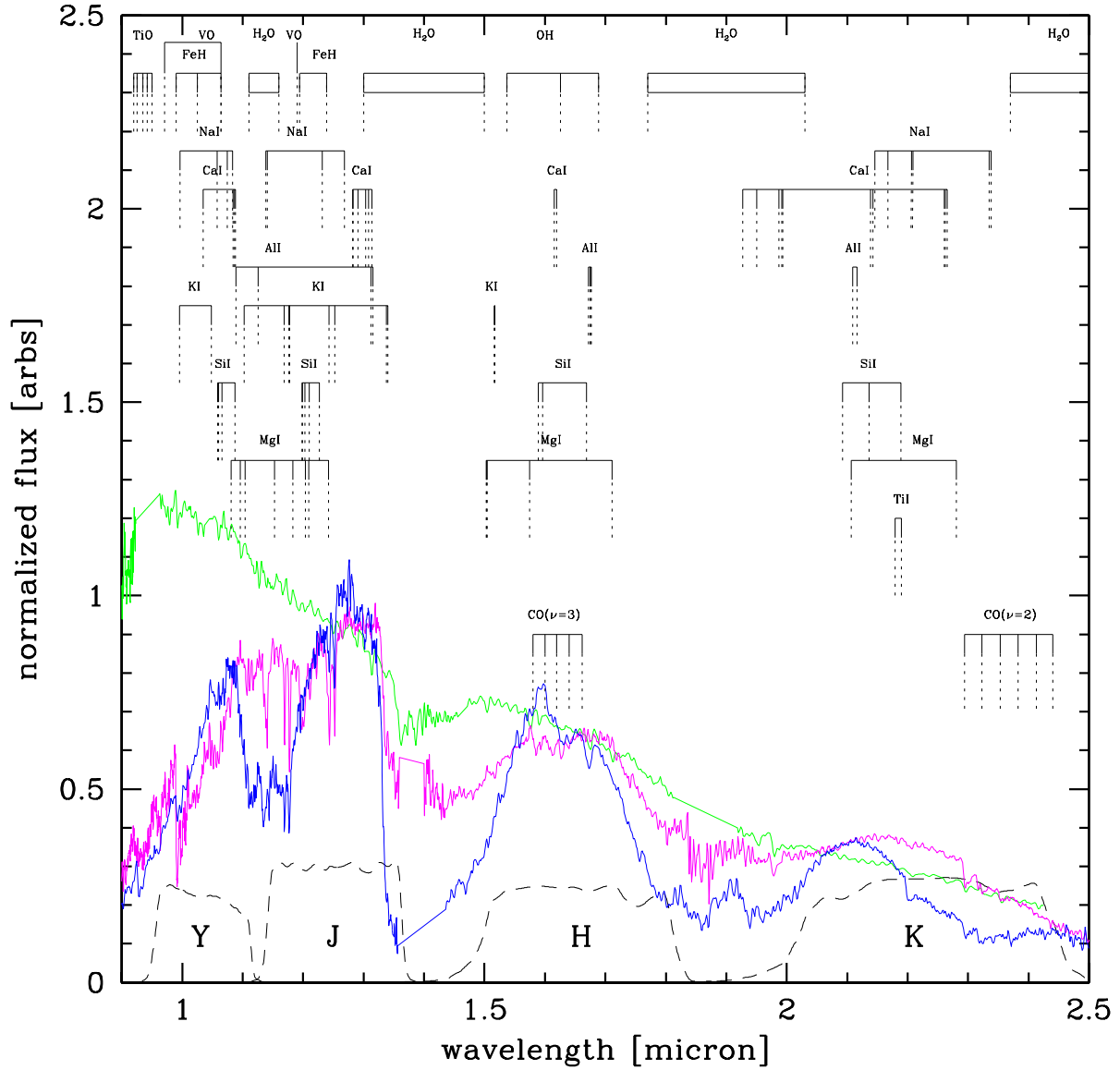


Fig. 2.— Near-infrared Y, J, H, and K filter transmission profiles (same as in Figure 1) superposed on the near-infrared spectra of LHS 386 (M1V; top), 2MASS 0746 (L0.5V; middle), and SDSS 1254 (T2V; bottom) from Leggett et al. (2000ab) and Geballe et al (2002). Top/middle/bottom refers to flux in the H₂O bands in between the filters; the spectra are arbitrarily normalized at 2.1 μm . Contributors to spectral absorption features are identified. The near-infrared Y-band is located near the peak flux of stars ~ 3000 K in temperature ($\sim M4.5$ - $M5V$ in spectral type). The peak flux shifts into and remains in the J-band at cooler temperatures down to 500 K (Burrows et al., 2001) suggesting that Y-J colors may continue to increase relative to Vega’s zero color even though Y-H and Y-K (in addition to J-H and H-K) colors turn blueward for T dwarfs.

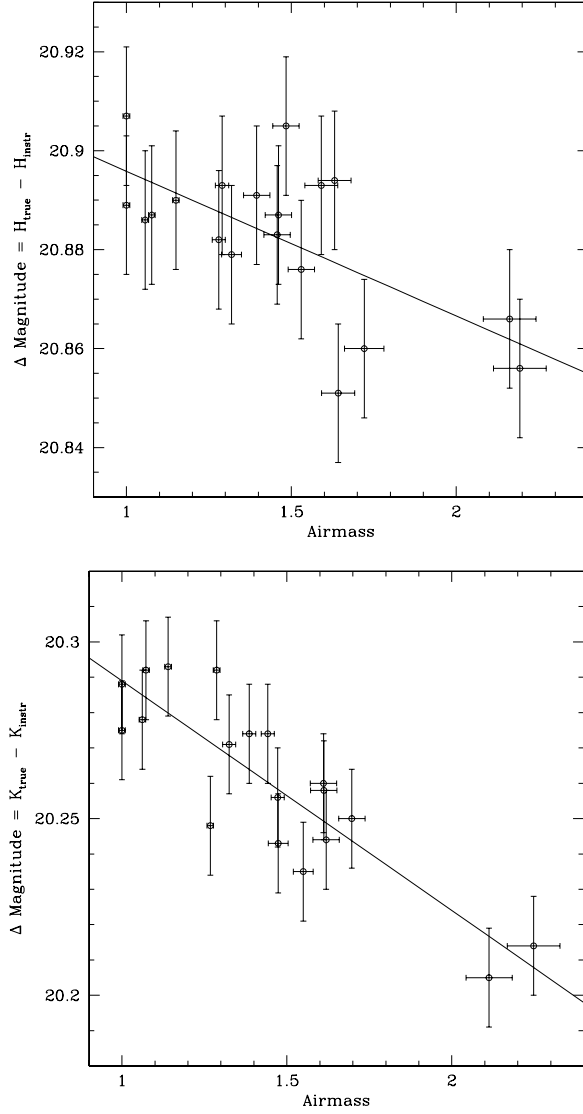


Fig. 3.— Calibration curves for H and K photometry obtained with the Palomar 60” telescope and P60/IRC. See text for equations describing the linear fits.

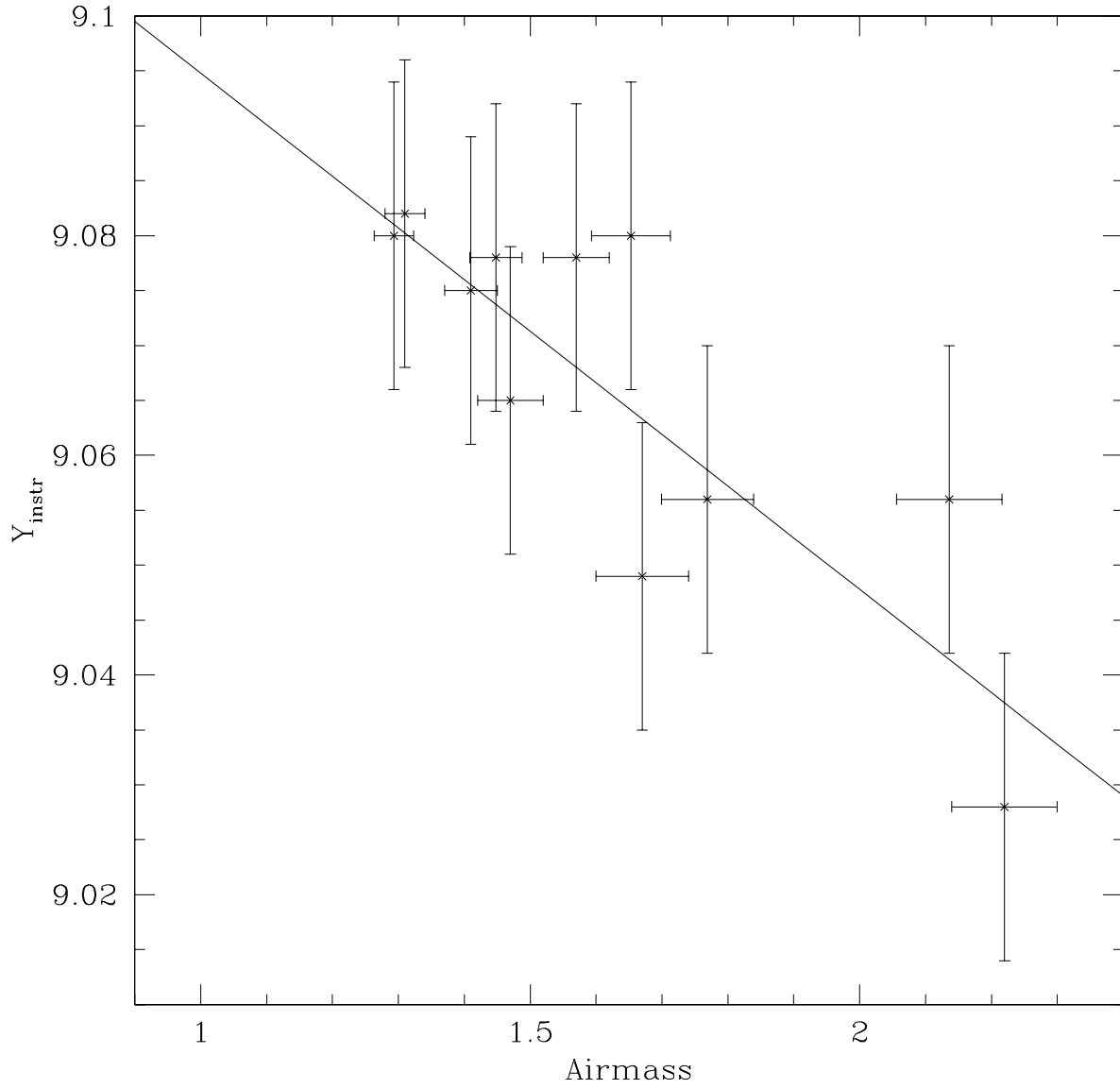


Fig. 4.— Instrumental magnitude in the Y filter vs airmass for GSPC S813-D. Data for both nights on which P60/IRC data were obtained was combined, with the second night's values shifted by 0.035 mag to produce the lowest error in the linear fit.

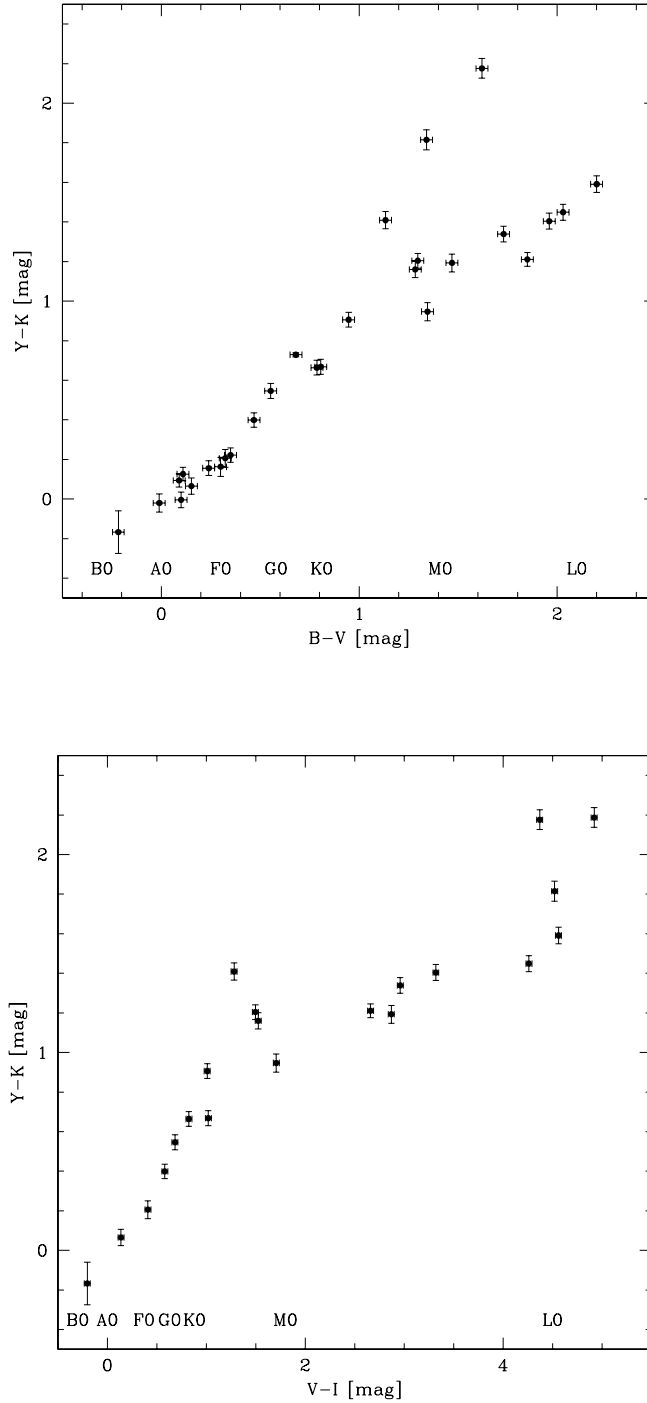


Fig. 5.— New near-infrared Y-K colors compared to optical B-V (top panel) and V-I (bottom panel) colors from the literature. Locations of spectral type labels correspond to optical colors. The reddest stars in Y-K with published optical photometry appearing in these figures are 2MASSW 1439284+192915 (L1 in the V-I plot only, with $Y-K = 2.19$) LHS 2924 (M9, with $Y-K = 2.18$), LHS 3003 (M7 or perhaps later, with $Y-K = 1.82$), and VB 8 (M7 with $Y-K = 1.59$). B-V colors appear to saturate and turn blueward around spectral type M7 while V-I colors saturate around spectral type M8 but do not turn systematically blueward at late types.

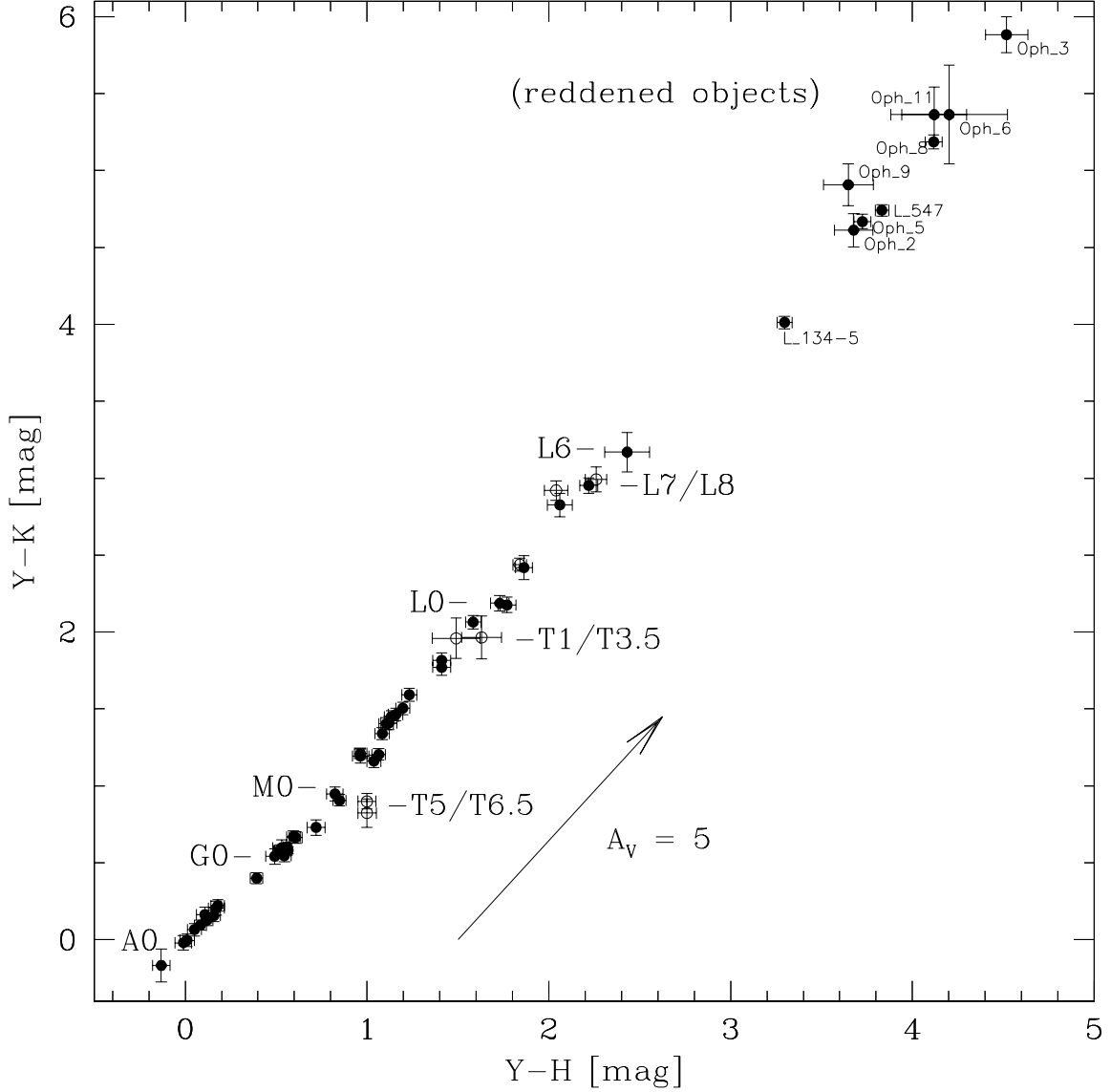


Fig. 6.— Newly derived Y-K vs Y-H colors for all stars in our sample plus Gl229b data from Matthews et al. (1996) taken through similar filters in the P200/D-78 camera. Dwarf colors steadily redden from the earliest type stars through at least spectral type L6 stars and brown dwarfs, though become increasingly bluer from L7 through at least T5. The spectral type labels correspond to Y-K colors; filled symbols indicate increasing color with advancing spectral type (labelled on the left of the sequence) and open symbols indicate decreasing color with advancing spectral type (labelled to the right of the sequence). All objects with Y-H and Y-K colors > 3.5 mag are substantially reddened; the derived magnitude and slope of the interstellar reddening vector are indicated by the arrow.

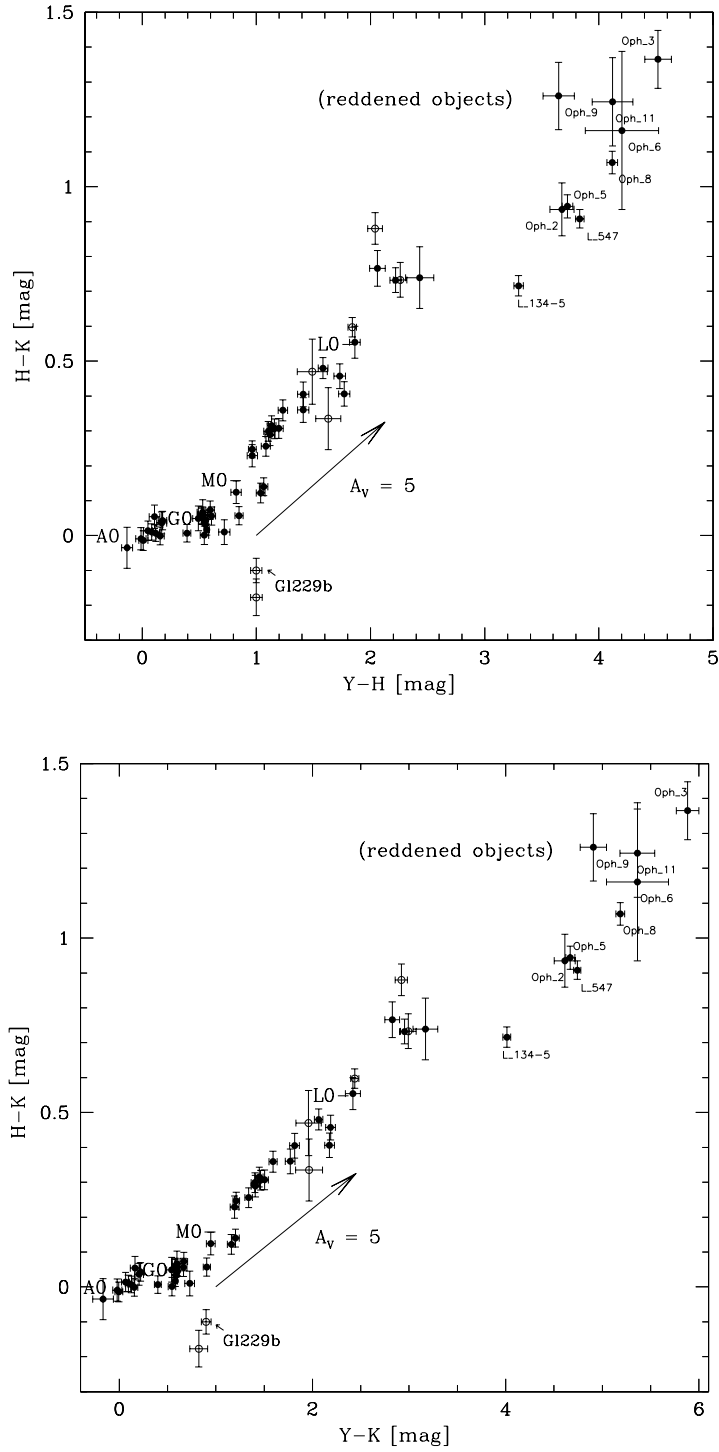


Fig. 7.— H-K colors vs Y-H (top) and Y-K (bottom) colors, similar in other ways to Figure 6. The centers of the spectral type labels correspond to H-K colors. H-K colors are relatively flat through spectral type K7 and then redden to ~ 0.75 by L6, flatten to L8, and turn blueward at later types. Y-K and Y-H colors redden more rapidly than H-K, though all YHK colors turn blueward by late L and into the T spectral range.